Application Notes

Design Materials with Specific Applications

Titanium alloys are metals which contain a mixture of titanium and other chemical elements. Such alloys have very high tensile strength and durability (even at extreme temperatures). They are light weight, have extraordinary corrosion resistance and the ability to withstand extreme temperatures. However, the high cost of both raw materials and processing have limited so far their use in military applications, aircraft, spacecraft, medical devices, connecting rods on expensive sports cars and some premium sports equipment and consumer electronics. Auto manufacturers Porsche and Ferrari use titanium alloys in engine components due to its durable

fight aircraft

Guggenheim Museum, Bilbao, Spain

| *The challenge:*	Identify orientation of a variants with respect to the mother phase
Solution:	ASTAR technique coupled with precession electron diffraction

properties in these high stress engine environments.

Although "commercially pure" titanium has acceptable mechanical properties and has been used for orthopedic and dental implants, for most applications titanium is alloyed with small amounts of aluminum and vanadium, typically 6% and 4% respectively, by weight. This mixture has a solid solubility which varies dramatically with temperature, allowing it to undergo precipitation strengthening. This heat treatment process is carried out after the alloy has been worked into its final shape but before it is put to use, allowing much easier fabrication of a high-strength product.

Nowadays, new titanium alloys are being designed, using cheaper elements as alloying elements. For example, Vanadium is replaced by Molybdenum or Niobium. This new alloy family is called Low Cost Beta (LCB) because of the stabilization at high temperature of the b bcc phase, giving rise to many variants of a hcp phase. These new compositions allow titanium alloys to be developed towards new applications such as in architecture (see the Guggenheim museum in Bilbao) where the exceptional properties of the alloy give rise to new shapes that defy gravity!
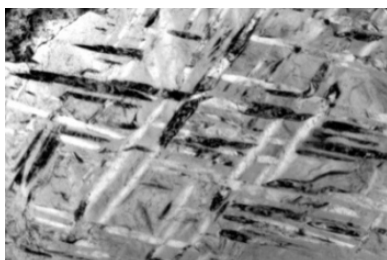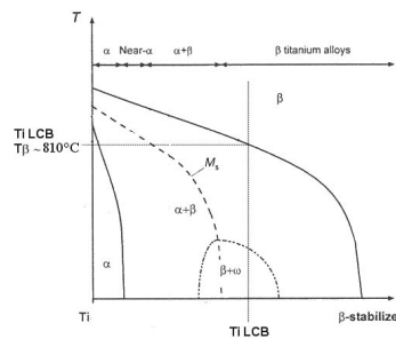
Crystal Structure

Ti α-phase:
Hexagonal P6$_3$/mmc
a=2.97 Å, c=4.72 Å
Ti β-phase:
Cubic Im$\bar{3}$m
a=3.28 Å

0.2 μm

Red = β Green = α

(111) Pole figure

0.2 μm
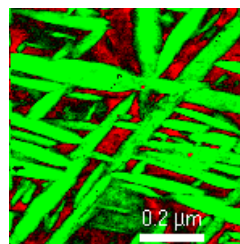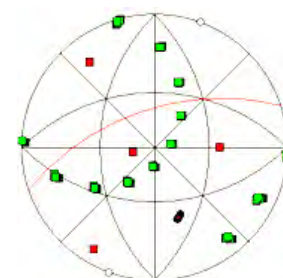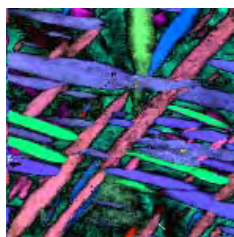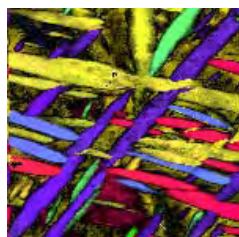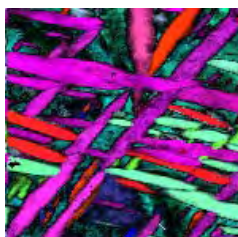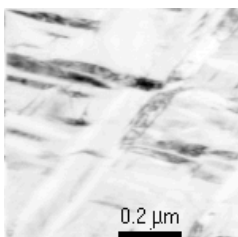
Experimental Data

TEM type: Jeol 2100F
Map resolution: 5 nm
Spot size: 1.6nm
Scanned area: 750x750nm

figure 1   (A) Ti alloy bright field TEM image (B) ASTAR phase map (C) ASTAR orientation map at nm scale   z direction, (d) x direction, (e) y direction

Better Steels with Improved Properties

Steel is an alloy made by combining principally iron and carbon, moreover other alloying elements are used to improve mechanical characteristics, such as manganese, or vanadium. The resulting steels are commonly know as High Strength Low alloy Steels (HSLA).

Carbon and other elements act as a hardening agent, preventing dislocations in the iron atom crystal lattice from sliding past one another. Varying the amount of alloying elements and the form of their presence in the steel (solute elements, precipitated phase) controls qualities such as the hardness, ductility, and tensile strength of the resulting steel. To harden a material, and especially a ferritic steel, it is also important to control the grain size, through cold rolling and recrystallisation processes.

The challenge: Identify orientation in deformed steels to measure grain size, and identify martensitic phases in stainless steels

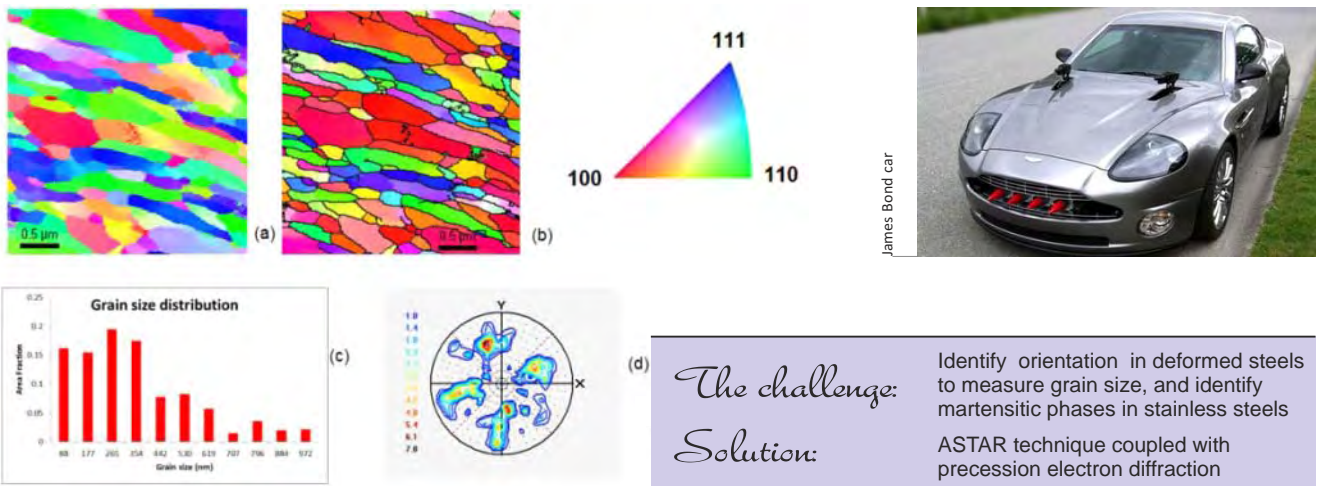**Solution:** ASTAR technique coupled with precession electron diffraction

figure 1

Grain refinement analysis in severely deformed pure iron. Orientation map with the color related to (a) x axis, (b) z axis with grain boundaries highlighted, (c) grain size distribution and (d) {111} pole figure. The color code for the orientation maps is shown on the right

In metallurgy, stainless steel, also known as inox steel, is defined as a steel alloy with a minimum of 11% chromium content by mass. Stainless steel does not readily corrode, rust or stain with water as ordinary steel does. There are different grades and surface finishes of stainless steel to suit the environment the alloy must endure. Stainless steel is used where both the properties of steel and resistance to corrosion are required. Some austenitic stainless steels have the spectacular property to transform into martensite when deformed, providing a unique combination of very high strength and ductility.

During deformation in tension, martensitic phases are formed in austenite, giving rise to a spectacular work hardening effect. Phases are clearly seen and characterized with ASTAR.

Crystal Structure
Ferrite: cubic, a = 2.86 Å
Austenite: cubic, a = 3.59 Å
ε-martensite: hcp
Martensite: Cubic, a= 2.86 Å

Experimental Data
TEM type: CM 200
Map resolution: 10 nm
Scanned area: 5 x 5 µm
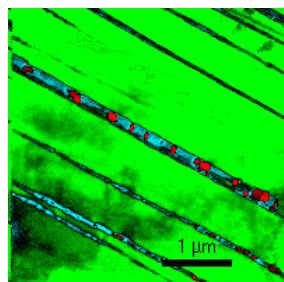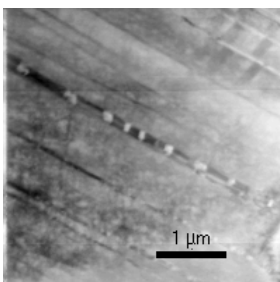
figure 2

TRIP 304 steel : Green = austenite fcc, Blue = e- martensite, red = martensite.

Challenging Materials for Challenging Applications

Synthetic Sapphire is a single crystal form of corundum, Al_2O_3, also known as alpha-alumina, alumina, and single crystal Al_2O_3. Synthetic sapphire is the hardest of all known oxide crystals with a 9 on the Mohs scale. It is second in hardness only to diamond, and retains its strength at high temperatures. Synthetic sapphire crystals have good thermal properties, with excellent electrical and dielectric properties. In addition, it combines zero porosity with near total resistance to acids and alkaline substances. In its purest form, no porosity or grain boundaries are present, making it theoretically dense. The combination of favourable chemical, electrical, mechanical, optical, surface, thermal, and durability properties make sapphire a preferred material for high performance systems and component designs. Due to these benefits sapphire has been used in various applications, such as sapphire wafers, lenses, substrates, watch glasses, and sapphire boule for many years. Synthetic sapphire is anisotropic hexagonal crystal. Its properties depend on crystallographic direction (relative to the optical C-axis). For various semiconductor applications, sapphire is the best choice in comparison to other synthetic single-crystals.

synthetic sapphire

luxury watch

The challenge:	Being able to identify correctly orientations in Al_2O_3 to study defects
Solution:	ASTAR technique coupled with precession electron diffraction

Sapphire is widely used for watch glasses. The world demand in the watch industry centres on scratchproof sapphire watch crystals. However, besides traditional flat shapes, crystals with spherical and cylindrical curves are also in great demand.

Did you know? Sapphire is the substrate for the growth of III-V and II-VI compounds such as GaN for LED's, used for LED.

Hip replacements

Another important application is the realization of hip prothesis, because of the biocompatibility and inert behaviour of sapphire in human bodies, combined with exceptional mechanical properties!

Thus, Analysis of polycrystalline sapphire, to understand the structure of defects and grain boundaries, was essential and was performed in high resolution using the ASTAR in combination with preccesion electron diffraction technique.

LED light

(A) 1 µm   **(B)**   **(C)**
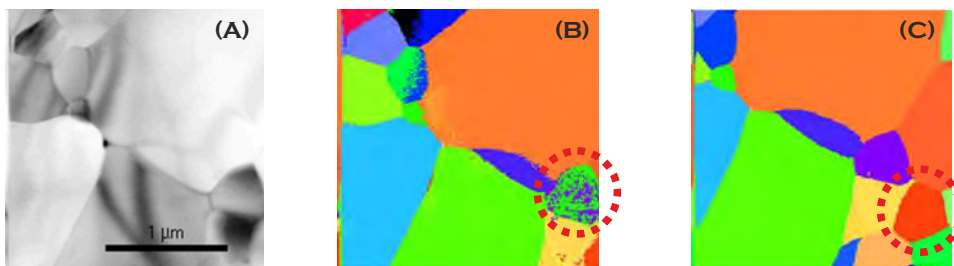
figure 1

(a) saphire grains (b) ASTAR orientation analysis without precession : orientation identification is poor, even wrong!
(c) ASTAR orientation map using 0.5° precession during acquisition allow to better capture Bragg reflection intensities and positions to analyze precisely grain orientations.
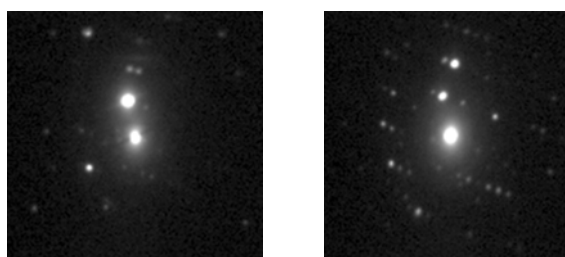
Crystal Structure

Al_2O_3: Trigonal, $R\bar{3}c$
a = 4.78 Å, c = 12.99 Å

Experimental Data

TEM type: Tecnai F20
Map resolution: 1 nm
Scanned area: 2 x 2 µm

Steel Corrosion in Nuclear Plants

Generation IV reactors (Gen IV) are a set of theoretical nuclear reactor designs currently being researched. Most of these designs are generally not expected to be available for commercial construction before 2030. Current reactors in operation around the world are generally considered second- or third-generation systems, with most of the first-generation systems having been retired some time ago.

Relative to current nuclear power plant technology, the claimed benefits for 4th generation reactors include:

- Nuclear waste that remains radioactive for a few centuries instead of millennia
- 100-300 times more energy yield from the same amount of nuclear fuel
- The ability to utilize existing nuclear waste in the production of electricity
- Improved operating safety.

Fourth generation reactors are not yet fully designed and current research is exploring among other solutions the ability to use liquid metals as caloporters. Embrittlement of steels with liquid metals is a known phenomenon, and an issue of crucial importance for this development. Here, liquid indium was put in contact with a carbon steel, and the resulting damage was investigated in relation to the microstructure of the bainitic steel. A fine analysis of all diffraction patterns allow to identify the presence of carbides at the crack tip as seen on the virtual bright field reconstructed with ASTAR.

While waiting for the 4th generation to be ready, it is important to study how Nuclear Centrals are ageing ! Here is reported some observation of aged stainless steels aged 55000 h (6 years and 3 months) at 600°C. The specimen was prepared using FIB technique to select a specific area containing ferrite phase.

nuclear power plant

(previously) liquid indium
Crack tip
Ferritic (bainitic) steel
VDF
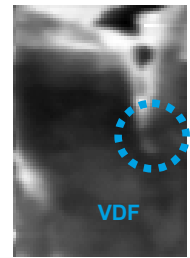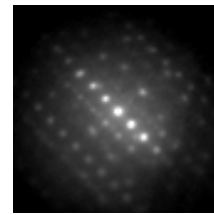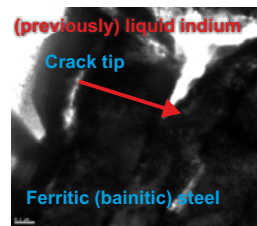
Crystal Structure

1	Bank_[fe bcc]_50_1_r3
2	Bank_[fe fcc]_50_1_r3
3	Bank_[Cr23C6]_50_0.3_r

The challenge:
Identify orientation / phase in a thick specimen

Solution:
ASTAR technique coupled with precession electron diffraction

1 µm

1 µm

figure 1

Analysis of all the FIB section (step of 20nm, size of the map : 16x6 µm to record) : ASTAR phase map combined with phase reliability. On the left, an austenitic grain is seen, on the right, a previously ferritic grain has decomposed into austenite and carbides.

blue = austenite fcc,
red = ferrite bcc,
green = carbides
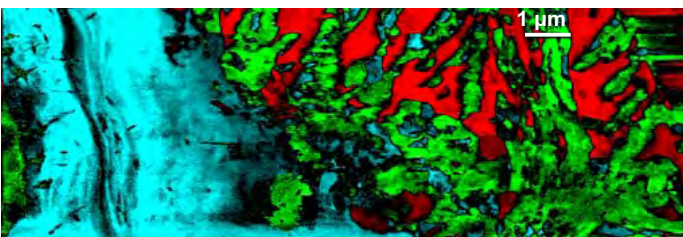
Experimental Data
TEM type: Jeol 3010
Map resolution: < 10 nm
Scanned area: 18 x 6 µm

Structure of Embedded Nanodomains in Intermetallics

Ni Te is an intermetallic compound with possible applications in thermoelectric generators (TEGs) that convert heat into electrical power by exploiting a temperature gradient. $Ni_{1+x}Te_1$ system is a two solid phase mixture where nanodomains of modulated (layered) unknown phase (phase b) were found inside the NiTe matrix. Despite many attempts to solve this unknown Ni Te phase b, its structure and stoichiometry was revealed only using 3D diffraction

The challenge:	Embedded nanodomains with size up to 70nm, two Ni Te phases
Solution:	Automated 3D Diffraction Tomography combined to Precession electron diffraction

tomography coupled to precession electron diffraction (PED).

3D diffraction tomography data were collected on the edge of a milled particle, revealed the presence of two phases, the matrix Ni_1Te_1 (phase α) and the superstructure Ni5Te4 (phase β). Structure determination of the modulated β phase was hampered by the small dimensions of the domains and the fact that most of them are embedded into the Ni_1Te_1 matrix. Reflections coming from the superstructure were recognized and showed a doubling of both c and a parameters, leading to an monoclinic. It is found out that is locally similar to NiTe, but there is a shift of one Te layer by (1/3, 1/3, 0) every two c-periods referred to the initial hexagonal NiTe-type structure.

The analysis of the experimental data confirms that Ni_1Te_1 (phase α) has a hexagonal structure, of NiAs type, where the Te atoms form a BCBC... hexagonal sequence. The remaining Ni atoms are distributed over octahedral sites between the Te Layers

embedded domains

50 nm

(figure 2).

The new Ni_5Te_4 (phase β) has a monoclinic structure where the Te atoms form a sublattice with BABCBA... hexagonal sequence, while the Ni atoms occupy deformed octahedral sites with a $...c_oc_oa_oa_oc_o...$ sequence and tetrahedral sites with a $...c_tb_tc_t...$ sequence. It is found out that is locally similar to NiTe, but there is a shift of one Te layer by (1/3, 1/3, 0) every two c-periods referred to the initial hexagonal NiTe-type structure.

ADT together with PED allowed the structure determination of the nickel-rich phase superstructure Ni_5Te_4 (phase β) for the first time.

Crystal Structure

Ni_1Te_1 (α phase)	Ni_5Te_4 (β phase)
Hexagonal P6$_3$/mmc	**Monoclinic Pm**
a= 3.85 Å	a= 6.95 Å
b= 3.85Å	b= 4.02 Å
c= 5.22 Å	c= 11.96 Å
α= 90°	α= 90°
β= 90°	β= 90°
γ= 120°	γ= 90°

Experimantal data

Ni_1Te_1 / Ni_5Te_4
tilt range: ±50° / ±40° step: 1°
No ind. reflections 47 / 411
No ind. atoms 2 / 11
R = 22.3% / 24.6%

figure 2

Crystal structure
Ni_1Te_1 (phase α)
and Ni_5Te_4 (phase β , down)

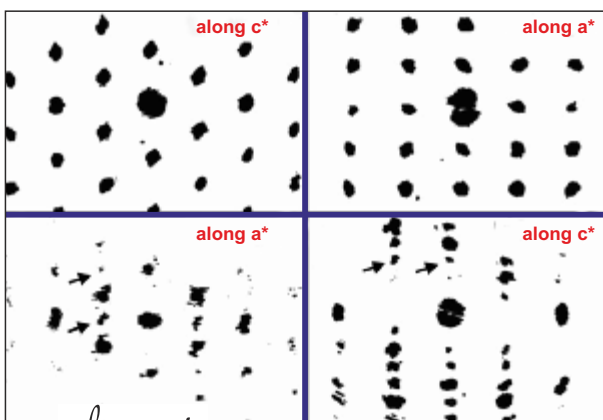## figure 1

Projections of the reconstructed 3D diffraction of phase α along the c* & the a* axis; (top, hexagonal) phase β along the c* & the a* axis (down, Moniclinic) Superstructure reflections are marked with Black arrows.

along c* along a*
along a* along c*

PRECESSION ELECTRON DIFFRACTION TOMOGRAPHY
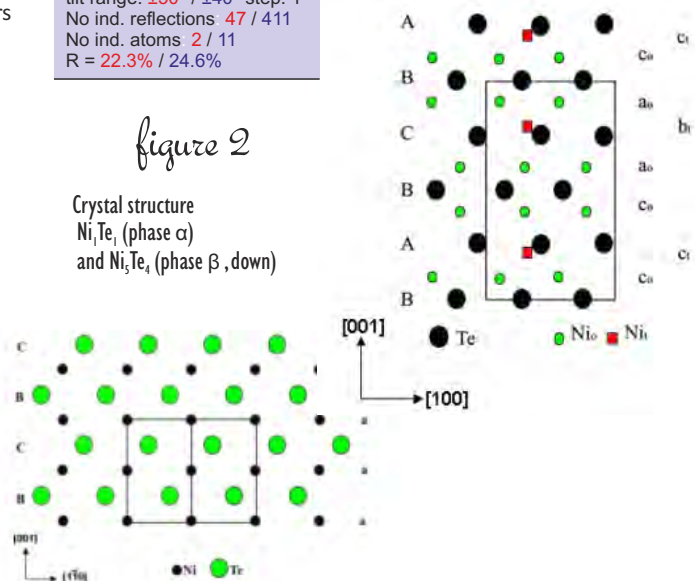
Metals under Huge Stress

Silver and copper have a wide miscibility gap therefore special methodologies are needed to obtain a metastable alloy. The usual results of a Cu-Ag alloy synthesis is spinodal decomposition of Ag, Cu phases intergrown in bands some hundred nanometers wide. A way to push the spinodal decomposition to a smaller scale is given by the severe plastic deformation induced by a high pressure torsion (HPT).

Several cycles of HPT mixed together the Ag and Cu bands in smaller grains of an Ag-Cu alloy. This process is extremely difficult to map in terms of phase separation, grain size and crystal orientation since it occurs on a nanometer scale.

The ASTAR technique can follow the processes in all phases. In the as cast starting mixture, an alternating sequence of Ag and Cu lamellae are detected. The orientation mapping reveals a strong orientation correlation between the lamellae. After one cycle of HPT the lamellar structure is hardly recognizable in planar view and becomes thinner and irregular in sections tangential to the deformation cylinder. The deformation induced by the torsion also changes the grain size and the texturing.

The challenge:	Identify orientation / phase of 2 different phases particles with < 50 nm
Solution:	ASTAR technique

Within each lamella some small grains with irregular shape start to appear. The orientation correlation between the lamellae is strongly reduced.

The process can be characterized with ASTAR at each step until a complete alloy is formed after 10 HPT cycles.

Copper tubes

Silver bars

Schematic Illustration of HPT process

Sample   (Φ=10mm)

+90°   -90°

1 cycle =   (90°) +   (-90°)
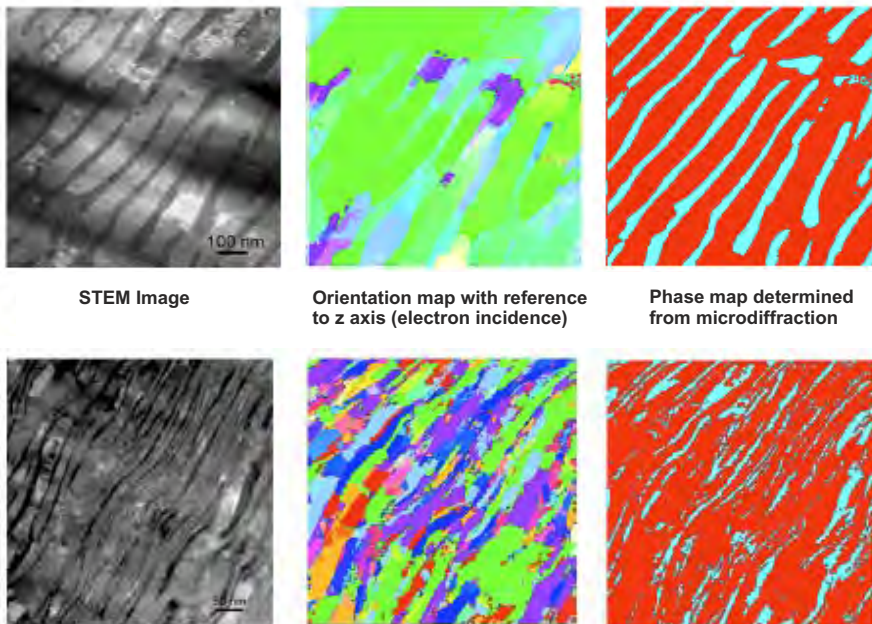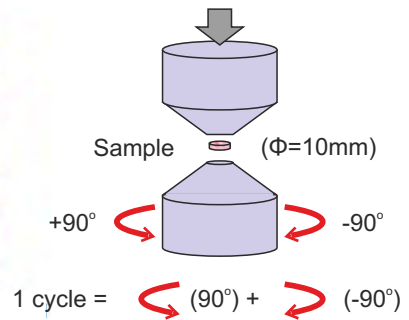
Crystal Structure
Silver: cubic, a = 4.086 Å
Copper: cubic, a = 3.615 Å

Experimental Data
TEM type: Tecnai F20 ST
Map resolution: 4 nm
Scanned area: 800 x 800 nm

STEM Image | Orientation map with reference to z axis (electron incidence) | Phase map determined from microdiffraction

Ag
Cu

figure 1

Top: The $Ag_{60}Cu_{40}$ eutectic mixture as cast. A regular spinoidal decomposition into Ag and Cu phase is easily detected by ASTAR.
Bottom: The same sample after one high pressure torsion treatment in tangential view. The spinodal decomposition bands become thinner and less corrected.

Pavements of the Nanoworld

Lisbon Pavement, Portugal

One effective method of producing nanocrystalline materials (grain size < 100 nm) is pulsed electrodeposition. It has been observed that electrodeposits form and grow in a nodular fashion each nodule representing a "colony" of nanosized grains (Cizek et al.). Orientation measurements performed in the vicinity of the boundaries separating two neighboring colonies suggest that the colonies in a nanocrystalline Ni-20% Fe electrodeposit might display a distinct ''cobblestone'' mesotexture characterized by a <001> fiber axis approximately perpendicular to the local curvature of the colony growth surface.

TEM has been used to investigate the local microtexture and misorientation characteristics of nanosized grains comprising mesoscale colonies in electrodeposited Ni, Ni-20 % Fe, and Ni-50 % Fe materials. Optical microscopy revealed the presence of mesostructure colonies in all three Ni-based electrodeposits studied. Consequent TEM analysis on specimen sections parallel either to the Deposition Plane (DP) or the Deposition Direction (DD) provided the size and shape distribution of the nanograins for all the materials studied.

ASTAR analysis indicated that both the bulk texture and the local microtexture and mesotexture of the as-deposited specimens are dominated by the <001>//DD fiber, which has also been observed in many other experimental studies.
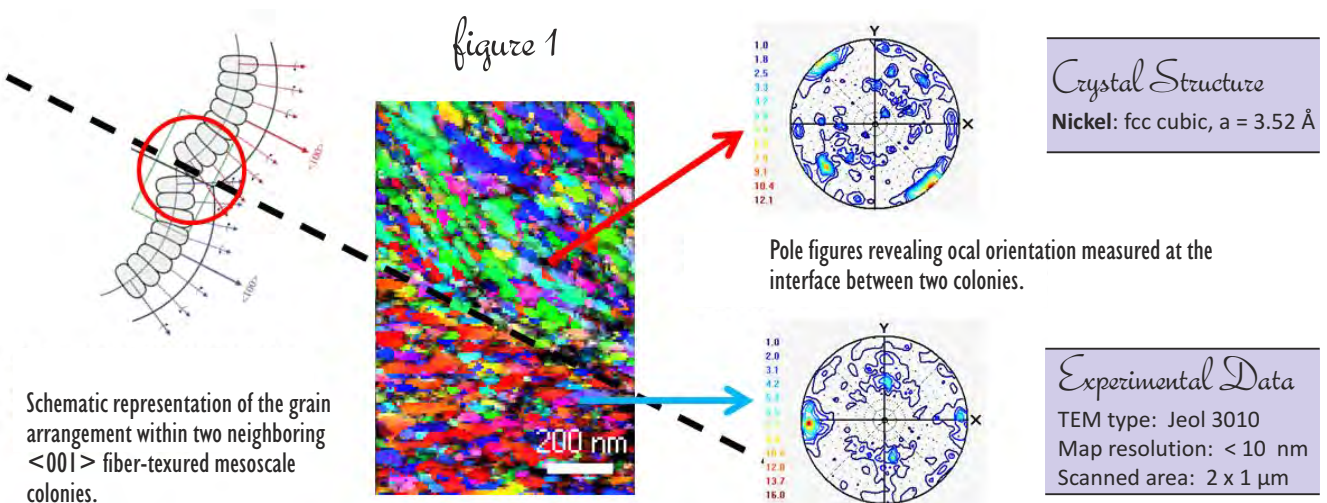
The challenge:	Identify the orientation of crystallites with size < 50 nm
Solution:	ASTAR technique coupled with precession electron diffraction

Researchers attribute this fact to the influence of hydrogen co-deposition which is more active in {001} than {111} crystallographic planes. For all three alloys, the coarsened grains, obtained by annealing, within the mesoscale colonies showed with EBSD-SEM a fiber mesotexture characterized by a <111> axis approximately perpendicular to the colony hemispherical growth surface (parallel to the local DD). From such EBSD-SEM measurements it has been surmised that the as-deposited texture patterns in Ni-based materials might resemble the patterns often seen in cobblestone pavements found in many European cities. This has indeed been confirmed by ASTAR orientation measurements made on a local nm scale in the as-received materials (see the figure below). Further work is needed to reveal the exact formation mechanisms of this cobblestone mesotexture as the aforementioned features will likely affect both the homogeneity and anisotropy of mechanical and physical properties of the nanocrystalline electrodeposits and many properties such as corrosion resistance, toughness or ductility, coefficient of friction and wear resistance could be affected by the characteristics of the mesoscale colonies.

figure 1

Schematic representation of the grain arrangement within two neighboring <001> fiber-textured mesoscale colonies.

Pole figures revealing ocal orientation measured at the interface between two colonies.

Crystal Structure
Nickel: fcc cubic, a = 3.52 Å

Experimental Data
TEM type: Jeol 3010
Map resolution: < 10 nm
Scanned area: 2 x 1 μm

Cizek et al *Metall. Mater. Trans. A* 42 (2011) 2048-2060

Understanding the
Li insertion / extraction mechanism
at microscopic level is important to
design next generation batteries

Understanding Li Insertion Mechanism for Next Generation Batteries

Lithium iron phosphate ($LiFePO_4$) is a good candidate for positive electrodes in lithium-ion batteries to be installed in new electric vehicles. Its cost is low, it has an excellent life cycle and it is safe. To obtain the best performances in terms of electrical conductivity it is synthesized in nanocomposite with grain size between 50 and 300nm.

The discharge-charge mechanism implies a delithiation of $LiFePO_4$ into $FePO_4$ and a successive insertion of Li into the iron phosphate. The mechanism of Li insertion / extraction at the microscopic level wasn't confirmed and at least four different models have been proposed.

The difference between the various models lies in the relative position, shape and dimension of the two phases, $LiFePO_4$, $FePO_4$ during the process. Two of these models imply core shell structures (bulk or radial), another one a spinoidal decomposition at the nanoscale level of two Li and Fe rich end members (spinoidal model), and the last one where the nanoparticles are either fully lithiated or fully delithiated (Domino-cascade model).

A phase mapping technique able to identify the lithiated and delithiated phase at the nanoscale can obviously solve the dilemma. Unfortunately the problem is complicated by the very similar unit cell parameters of $LiFePO_4$ and $FePO_4$ which differ from each other by less than 5%. ASTAR system can solve the problem by collecting the NanoBeam Electron Diffraction (NBED) patterns in precession mode.

Precession diffraction, on the one hand reduces the dynamical effects so that the patterns are closer to a kinematical simulation of the templates and on the other, it en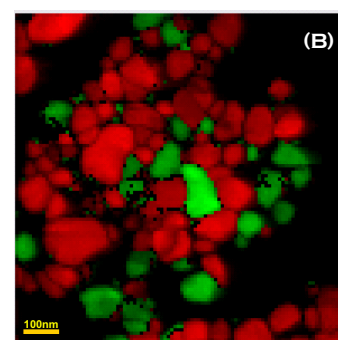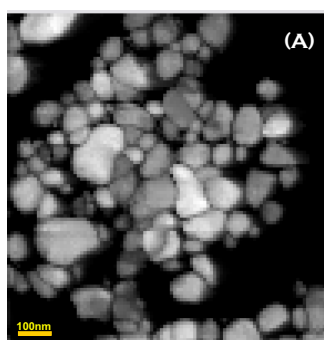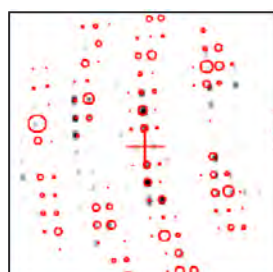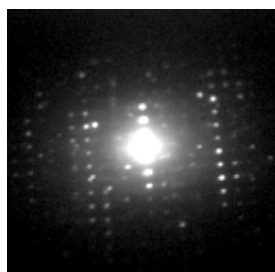ables the collection of a higher number of reflections from high order Laue zones reducing the ambiguity in indexing the patterns. In this way ASTAR system has been able to detect that the nanocrystalline grains of the nanoparticles are either fully lithiated or fully delithiated giving strong support to the domino-cascade model (fig. 2). The results have been confirmed also using HRTEM imaging and EFTEM / EELS analysis.

Enviromental friendly energy sources

The challenge:	Identify Li doped particles between two different phases having <5 % difference in cell parameters and particle size <50 nm
Solution:	ASTAR technique coupled with precession electron diffraction

Crystal Structure

$LiFePO_4$: Orthorhombic
a=10.33 Å, b=6.01 Å, c=4.69 Å
$FePO_4$: Orthorhombic
a=9.81 Å, b=5.79 Å, c=4.78 Å

Experimental Data

TEM type: Jeol 2010 FEF
Spot size: 2.7 nm
Step: 5 nm
Scanned area 1 x 1 μm

figure 1

Experimental precessed patterns and its indexation with the $LiFePO_4$ (red) and $FePO_4$ (green) templates with the corresponding agreement factors.

| 🟥 | **$LiFePO_4$** | 🟩 | **$FePO_4$** |

figure 2

Reconstructed bright field image (a), phase determination map (b).
Crystal grains of the nanocomposite mixture of $LiFePO_4$ (red), $FePO_4$ (green) during different phases of the charge-discharge cycle.
There is no mixing of the two phases inside the same crystal grain.

Nanoscale Reaction Models in Solid Oxide Fuel Cells

Solid oxide fuel cell (SOFC) technology is a promising energy conversion option at a time when efficient solutions are sought. During the electrochemical reaction of a fuel with an oxidant gas (usually air) at an operation temperature of ~ 800°C, SOFCs cogenerate heat and electricity with high efficiency: Electric efficiencies close to 60% are obtained now with a SOFC alone. When coupled with a micro gas turbine (SOFC-GT), these can increase up to 70%. Advantages of SOFCs also include flexibility of fuel use (e.g. CO, H_2, CH_4), delocalization of energy conversion, and reduction of pollutants such as NO_x and SO_x.

Hydrogen Fuel Cell component

A SOFC is composed of three main components: an anode, an electrolyte and a cathode. The standard design is based on the use of a porous ceramic-metal (cermet) composite anode made of yttria (Y_2O_3)-stabilized zirconia (YSZ) and Ni .

The anode acts as a fuel oxidation catalyst, hydrocarbon reforming catalyst, current collector and often as a mechanical supporting layer of the whole fuel cell. NiO particles are sintered with YSZ and then reduced by the fuel to metallic Ni during the first operation of the cell. During service life, minimum 5 years at ~ 800 °C, the anode runs on fuel and Ni is kept in its reduced state.

In this project, environmental transmission electron microscopy (ETEM) is used to understand the reaction mechanisms and the structural evolution of the as-sintered NiO-YSZ anode during reduction. A thin window, which is prepared using a dual beam FIB/SEM, is reduced inside the ETEM in a total pressure of 1.3 mbar of H_2. NiO reduction is observed to start at the grain boundaries with the YSZ phase. Pores form within the NiO grains to accommodate the volume shrinkage linked to the removal of oxygen. A post mortem analysis using ASTAR orientation imaging allows monitoring of the crystallographic changes induced by reduction at nm scale. It can be seen that the reduced Ni grains maintain the same orientation as the initial NiO grains, while the YSZ phase is left unchanged by the reaction. Based on these observations, reaction models can be established.

The challenge: Monitoring crystallographic changes after reduction of fuel cell: orientation / phase of two different phases with details of 1 nm

Solution: ASTAR technique coupled with precession electron diffraction

Crystal Structure

Y_2O_3: Cubic, Ia$\bar{3}$, a = 10.58 Å
NiO: Cubic, Fm$\bar{3}$m, a= 4.168 Å
Ni: Cubic, Fm$\bar{3}$m, a = 3.52 Å

Experimental Data

TEM type: Jeol 2200 FS
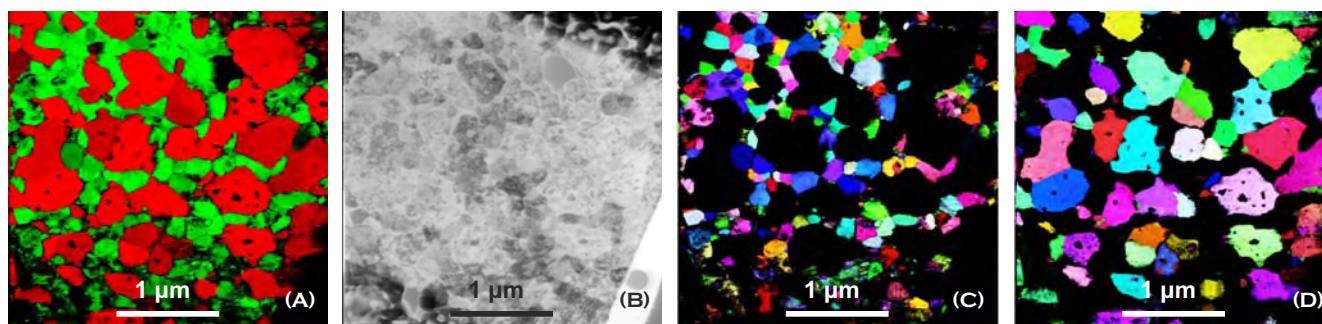Map resolution: 1   nm
Scanned area: 4 x 4 µm

figure 1

(A) ASTAR phase map where both NiO phase (red) and YSZ phase (green) can be seen
(B) same area TEM bright field image
(C) ASTAR orientation mapping for NiO phase and (D) ASTAR orientation map for YSZ phase.

Atomic Scale of Nanolayer Composites

A stacking fault is a one or two layer interruption in the stacking sequence of the crystal structure. These interruptions carry a certain stacking fault energy (SFE).

High SFE materials such as Al do not form twins easily. However, researchers have shown that it is possible to form Al layers in twin orientation to each other across polar TiN layers, if these are grown so that both the Al and TiN layers have a {111} surface as their growth front. Al-TiN multilayers were deposited at room temperature on Si substrates using dc magnetron sputtering in the two following different layer thicknesses: Al-9nm/TiN-1nm .

HREM-STEM image I collected by a HAADF detector, showed two Al layers separated by a TiN layer. It was seen that the Al layer is always the one that has a twin orientation with respect to the TiN and Al layers below it. The situation is schematically illustrated in the figure below. Theoretical ab initio calculations based on density functional theory (DFT) revealed that nitrogen termination in the {111} growth plane of the TiN layers greatly favors the growth of twin oriented Al layers on them, thus, being in excellent agreement with experimental observations.

In conclusion, it was shown that in magnetron sputtered Al-TiN multilayers, consecutive Al layers grow in twin orientation with respect to each other when the intervening TiN layers are 1–2 nm thick.

The above HREM experimental data were explored further by means of the ASTAR system that was able to produce orientation / phase maps of the Al-TiN nanolayers revealing clearly the TiN layer of 1 nm thickness. ASTAR orientation maps show clearly the twin orientation relationship between succesive Al layers.

Moreover, these findings suggest a method of introducing nanoscale twins in high SFE materials in general. Since the deposition of Al and TiN layers is used in the formation of diffusion barriers, it is important to investigate and understand these structures at the nanometer length scale and hence to be able to control them.

Binary code

The challenge:	Identify orientation / phase of 1 nm TiN layer in a Al-9nm / TiN-1nm nanolayer composite while TiN and Al differ <5% in cell parameter
Solution:	ASTAR technique coupled with precession electron diffraction
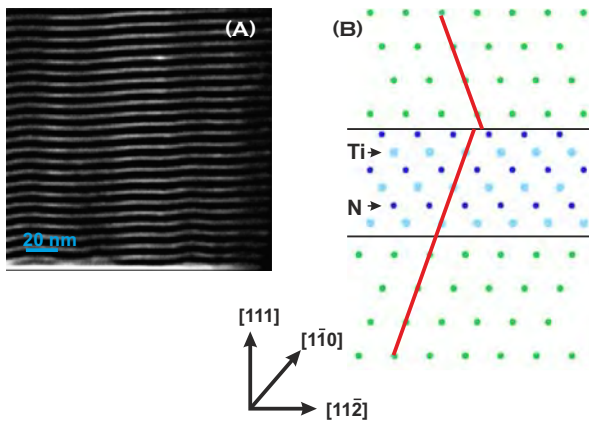
Crystal Structure
Al: fcc cubic a = 4.05 Å
TiN: fcc cubic a = 4.24 Å

Experimental Data
TEM type: Jeol 2100 F
Map resolution: 1 nm
Scanned area: 200 x 200 nm

figure 1
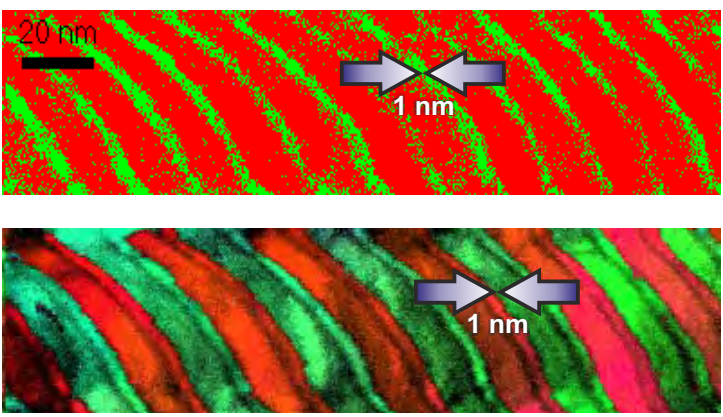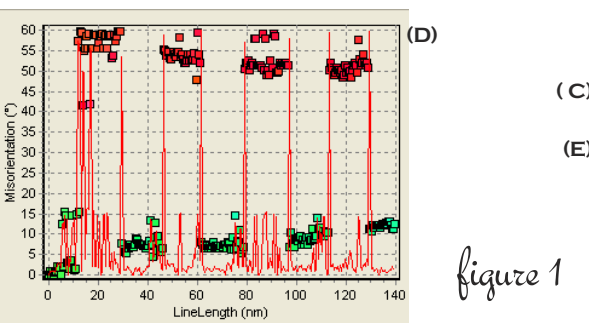
(a) HAADF image of Al-9nm/TiN-1nm multilayer system (b) atomic model of the Al-TiN-Al interface (c) ASTAR orientation map where Al layers are shown in red, TiN 1nm layer shown in green (d) line profile of ASTAR orientation map showing twin-related Al layers (E) ASTAR orientation map with 1nm TiN layers shown as black strips

Next Generation Circuits for Semiconductor Industry

Semiconductor Industry

Circuit with microprocessor

Computer wafer

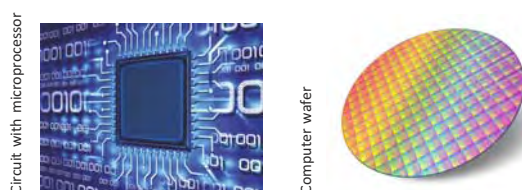The scaling required to reach faster chip performances in electronic devices has pushed the dimensions of copper interconnect (CI) lines to the nanometer domain. This constant downscaling of CIs implies a change in their microstructure. A change in the grain boundary type distribution and local texture will strongly influence the resistivity and the mechanical reliability of downscaled CIs. A different texture can imply different mechanical properties and a different local distribution of stresses. It is, therefore, necessary to map the texture evolution with the size of CIs.

Unfortunately, CIs that reach lateral sizes of less than 100 nm, with Cu grains smaller than 50 nm, cannot be characterized by conventional techniques like EBSD and XRD, because they do not have enough spatial resolution.

For reliable texture quantification, it is important to acquire extensive and reliable data sets to have statistically meaningful results and at the same time have a high spatial resolution. ASTAR with a parallel nano-sized beam, coupled with a small precession angle, has the appropriate spatial resolution (1 nm) and the reliable pattern indexing which reduces the 180° ambiguities by sampling reflections from higher order zones (HOLZ). In addition, ASTAR is able to acquire data and index patterns rapidly, which makes it possible to acquire statistically relevant information.
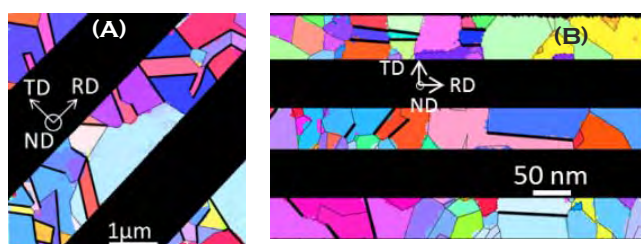
The challenge:	Characterize Copper Interconnect lines (CI) grain boundaries and texture at 1nm scale
Solution:	ASTAR technique coupled with precession electron diffraction

ASTAR orientation maps reveal the evolution of texture as the CI are scaled from CIs from 1.8 μm to 70 nm. In large CIs the Cu grains have a strong <111> fiber texture normal to the trenches (Fig. 1). In the smallest CIs, a <110> texture is observed, normal to the trench while {111} planes are now parallel to the trench sidewalls (Fig. 1). The microstructure also changes from a bamboo-like structure in large CIs into a polygranular structure in small CIs, where a polygranular microstructure is a microstructure in which there are continuous grain boundary paths along the length of the interconnect. In the 70 nm CIs grain size is not uniform and clusters of small grains are formed at the bottom of the trenches. Such clusters of small grains adversely affect the reliability of CIs. In addition, a decrease in the fraction of coherent twin boundaries was observed with d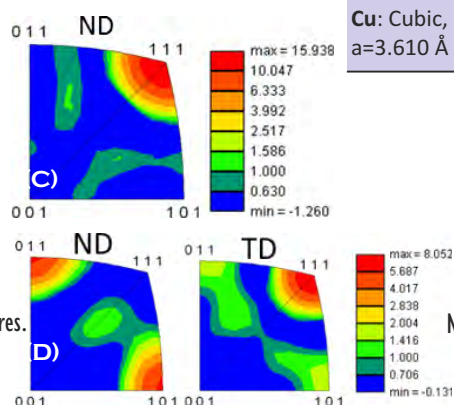ecreasing line widths (Fig. 2). Twin boundaries play an important role in the resistivity performance of CIs. These results are crucial to optimize the process of CI fabrication and to understand how to improve their mechanical and electrical properties.

figure 1

ASTAR orientation maps of CIs along with texture plots.
(A) shows the map from 1.8μm wide line.
(C) plot shows the distribution of crystal directions normal to the trench. Similar plots for the 70 nm wide lines are shown in (b) & (d) figures. Note the change in texture between the two line widths.

Experimental Data	TEM type: Jeol 2010 F Map resolution: 1 nm Scanned area: 2 x 2 μm
Crystal Structure	**Cu**: Cubic, Fm$\bar{3}$m a=3.610 Å

figure 2

Fraction of twin boundaries as a function of line widths. Note the decreasing twin boundary fraction as the line width decreases. Approximately 8000 boundaries extracted from orientation maps was used for this purpose.

Ganesh et al *Nanotechnology* 23 (2012) 135702

Structure of Magnetic Semiconductors

Magnetic semiconductor materials have attracted widespread attention in recent years due to their potential applications for the transport of information by exploiting both the intrinsic spin of the electron and its associated magnetic moment, in addition to its fundamental electronic charge. The new technology which emerged from discoveries in the 1980s concerning spin-dependent electron transport phenomena in solid-state devices was called Spintronics ('Spin Transport Electronics') also known as magnetoelectronics.

Spintronics

The material system (Mn,Ga)As on GaAs is of great interest for the development of such spintronic devices because the unstrained-bulk-MnAs is ferromagnetic at room temperature (α-MnAs, $P6_3/mmc$). It undergoes a phase transition to paramagnetic phases at 40°C (β-MnAs, Pnma) and above 125°C (γ-MnAs, $P6_3/mmc$)). "Surface contactable quasi-embedded" MnAs crystallite precipitates are formed in a [001] – oriented GaAs matrix during the cooling down stage of a MnAs layer that was deposited by metal-organic chemical vapor deposition (MOCVD) above 600 °C.

In order to obtain a thorough understanding of the (Mn,Ga)As crystallite formation process, the crystallographic phase and orientation of the precipitates with respect to the matrix have to be determined. The chemical composition of the precipitates was determined by quantitative EDXS analysis, their chemical composition was defined as $Mn_{0.75}Ga_{0.25}As$.
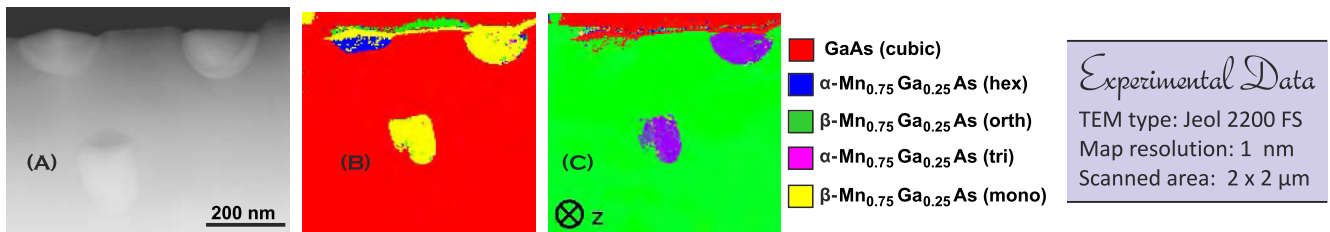
A careful inspection of the PED diagrams on the precipitates showed that there existed super structure reflections not consistent with MnAs bulk structure. ASTAR template matching analysis with all possible templates of 4 possible phases compatible with $Mn_{0.75}Ga_{0.25}As$

The challenge:	Identify unknown phase of MnGaAs precipitates among 4 different crystal phases & establish orientation relation between GaAs matrix and precipitates
Solution:	ASTAR technique coupled with precession electron diffraction

(total 38561 templates) shows a coexistence of precipitates with the monoclinic β-phase (space group $P2_1/m$) and of precipitates with the hexagonal α-phase ($P6_3/mmc$) at room tempereture. An example of ASTAR phase and orientation analysis of the embedded (Mn, Ga)As-crystallite precipitates in GaAs is illustrated below.

(A) (B) (C)

200 nm

⊗ z

- **GaAs (cubic)** (red)
- **α-$Mn_{0.75}Ga_{0.25}As$ (hex)** (blue)
- **β-$Mn_{0.75}Ga_{0.25}As$ (orth)** (green)
- **α-$Mn_{0.75}Ga_{0.25}As$ (tri)** (magenta)
- **β-$Mn_{0.75}Ga_{0.25}As$ (mono)** (yellow)

Experimental Data
TEM type: Jeol 2200 FS
Map resolution: 1 nm
Scanned area: 2 x 2 μm

(a) HAADF image of GaAs matrix and precipitates (b) corresponding ASTAR phase map (c) ASTAR orientation matrix along z (d) stereographic projection of monoclinic phase (e) orientation relation between GaAs matrix and the completely embedded (Mn,Ga)As crystallite & (f) stereographic projection of cubic GaAs

figure 1

Crystal Structure
GaAs: Cubic, F43̄m
a= 5.65 Å
$Mn_{0.75}Ga_{0.25}As$: hexagonal,$P6_3/mmc$
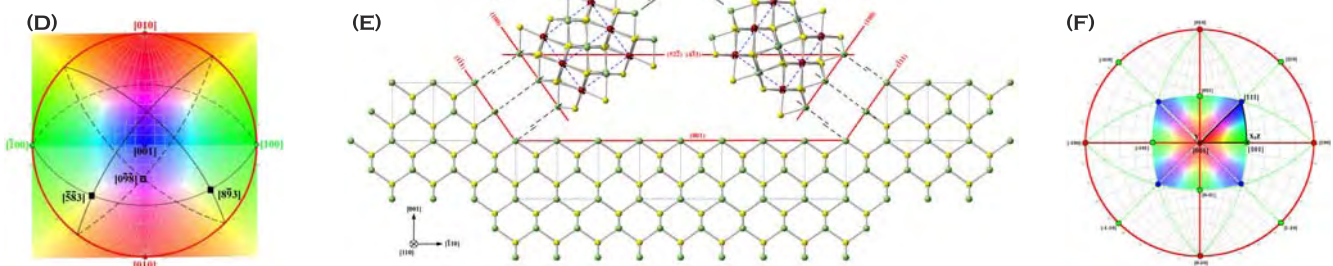
(D) (E) (F)

# Hybrid Inorganic / Organic Systems for Optoelectronics in Daily Life

Nanocrystalline ZnO is provided in an inorganic/organic system of ZnO deposited on sexiphenyl (6P).Initially 6P was deposited on a-plane ZnO substrate at room temperature forming mesoscopic 1-dimensional islands of 6P. In a second step, the islands were capped with ZnO via molecular beam epitaxy at 373 K.

Information on the nanostructure of ZnO grown atop 6P was provided by high-resolution TEM. Imaging was performed along the [00.1] direction of the ZnO substrate which showed that ZnO exhibits a perfect crystal structure when directly grown on the substrate. This was confirmed by Fourier transformation (FT) which also confirmed that ZnO grown atop 6P undergoes an imperfect growth.

Identification of the orientation of the nanocrystals and indexing of the lattice planes only based on FT is rather ambiguous and must be handled with care. For this reason, ASTAR was used to uncover any specifics of the overgrowth regime of ZnO on 6P at nm scale.

With ASTAR scanning the electron beam in nanobeam diffraction mode (probe diameter 1 nm) across an area of 100 nm in width and 80 nm in height provides the orientation maps depicted below. The maps were derived by comparing the diffraction pattern recorded at each individual position with a set of about 1000 calculated diffraction patterns of hexagonal ZnO. Focussing on ZnO atop 6P, columnar grains are identified that extend even up to the surface as signified by green and red areas.
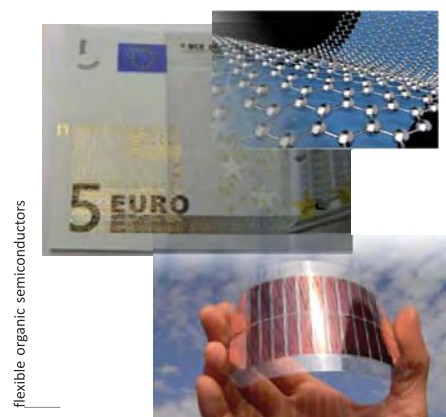
flexible organic semiconductors

| *The challenge:*	Identify precise orientation texture between ZnO substrate - sexipephenyl (6P) - ZnO deposited layer at nm scale
Solution:	ASTAR technique coupled with precession electron diffraction

From the ASTAR orientation map it is evident that the [00.1] wurzite axis is well-aligned along the vertical growth direction indicating a strong texture. Electrostatic forces originating from the 6P molecules have to be considered as the origin of this texture. In addition, a significant lateral texture within the (0001) plane cannot be excluded, as it cannot be distinguished which of the six prismatic facets contribute to the diffraction pattern.

Research on ZnO is of immediate practical importance as this semiconductor has several favorable properties, including good transparency, high electron mobility, wide bandgap, and strong room-temperature luminescence. These properties are used in emerging applications for transparent electrodes in liquid crystal displays, in energy-saving or heat-protecting windows, and in electronics as thin-film transistors and light–emitting diodes (LEDs).

ZnO

ZnO

ZnO

ZnO

(A) TEM — ZnO, 6P, ZnO — 20 nm

(B) orientation map
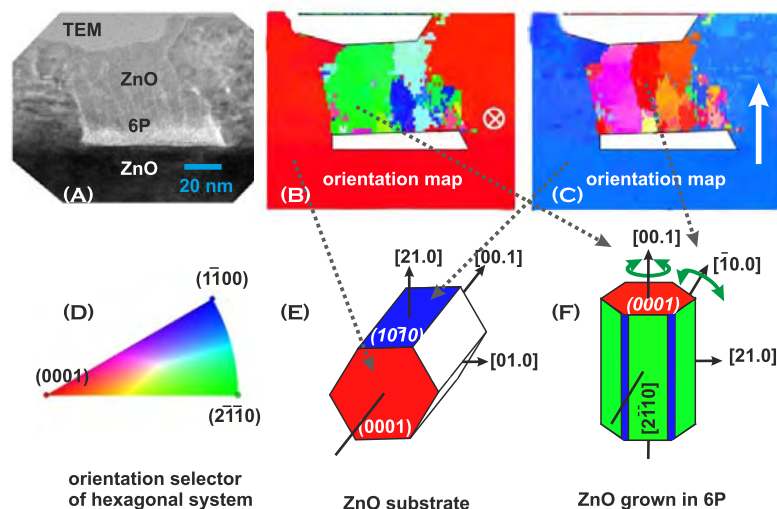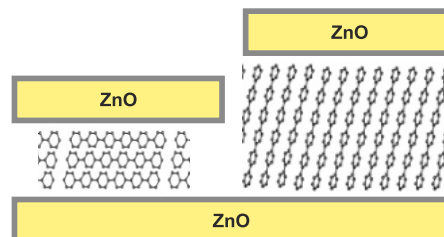
(C) orientation map

Crystal Structure
ZnO: Hexagonal, P6₃mc
a = 3.22 Å, c= 5.20 Å

Experimental Data
TEM type: Jeol 2200 FS
Map resolution: 1 nm
Scanned area: 100 x 80 nm

(D) orientation selector of hexagonal system — (1̄100), (0001), (21̄1̄0)

(E) ZnO substrate — [21.0], [00.1], (101̄0), [01.0], (0001)

(F) ZnO grown in 6P — [00.1], [1̄0.0], (0001), [21̄1̄0], [21.0]

figure 1
Crystallographic orientation mapping of ZnO as revealed by scanning nanobeam diffraction (SNBD):
a) TEM image of the region analyzed by SNBD.
b) and c) crystallographic orientation maps of ZnO. The white arrow markers represent the lattice planes color coded by the orientation triangle of d).
e) alignment of a representative ZnO unit of both, ZnO substrate and low temperature grown homoepitaxial ZnO,
f) alignment of a representative ZnO unit for the textured growth atop sexiphenyl.

23

Nanoparticle size and texture
are very important for
drug delivery of poor
water soluble drugs

Drug Delivery & Structure of Nanoparticles

Surgeons at work

Iron oxide nanoparticles (usually below 20nm) are being investigated for biomedical applications because of their biocompatibility and unique physical properties. This biocompatibility results from their capacity for metabolism, transportation and storage in human tissues. Magnetic iron oxide particles with diameters above 20nm are ferromagnetic, i.e. they have a reminiscent magnetic moment that generates unstable particulate suspensions, as the particles aggregate together into biologically toxic, micron-sized clusters.

Small Fe_2O_3 below about 20 nm are superparamagnetic, which means thermal energy is sufficient to cause large fluctuations of their magnetic moment, so that in the absence of an magnetic field, the particles have no effective moment. This reduces inter-particle attraction and makes stable, biocompatible suspensions possible. These particles maintain a strong response to an external magnetic field, which make them ideal candidates for biomedical applications, e.g improve effectively the poor water solubility of hydrophobic drugs.

Colloidal systems, including nanoparticles and liposomes, have been extensively studied as potential drug carriers for targeted or controlled release. Monitoring of the nano-assembly will facilitate an indirect determination of the site at which the therapy is administered.
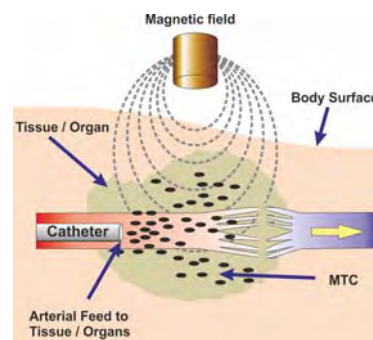
The texture of nanoparticles is therefore the utmost importance to control undesired agglomeration effects for drug delivery applications. ASTAR has been used in order to reveal succesfully 1 nm scale details of very small nanoparticles (Pt of 5-10nm in size and magnetite Fe_3O_4 parttcles of 100nm in size (figure 1).

The challenge:	Identify orientation textufe of very small <5nm nanoparticles & distinguish between particles of same cells but different space groups
Solution:	ASTAR technique coupled with precession electron diffraction

On the other hand, ASTAR has been used successfully to distinguish between a mixture of structurally closely related nanoparticle structures (e.g magnetite and maghemiite having essentially the same unit cell dimemsions but different space groups , see table).HR-TEM study is possible to use to distinguish between both phases,but is too time-consuming. Automatic ASTAR orientation / phase map analysis by comparing experimental PED patterns with both maghemite /magnetite templates , revealed higher reliability for magnetite crystals (results confirmed independently by HREM techniques). Collection of quasi-kinematical PED was essential to distinguish between patterns that belong to different Space Groups and extinctions may become visibe with ZOLZ – HOLZ reflections.

Magnetic field
Body Surface
Tissue / Organ
Catheter
MTC
Arterial Feed to Tissue / Organs

Crystal Structure

Magnetite Fe₃O₄: Cubic, Fd3m, a=8.32 Å
Maghemite γ-Fe₂O₃: Cubic P4₁32, a=8.33 Å

Experimental Data

TEM type: Tecnai 20 & Jeol 2010F
Map resolution: 1 nm
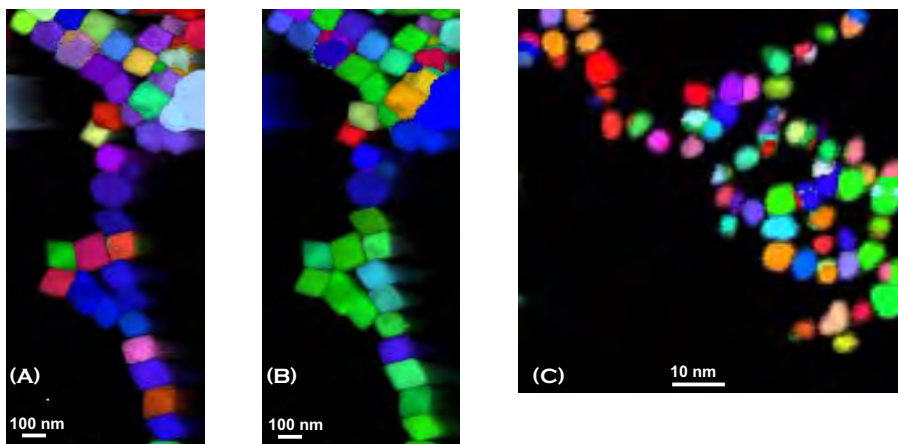Scanned area: 2 x 2 μm

(A) 100 nm

(B) 100 nm

(C) 10 nm

figure 1 (a) ASTAR orientation mapping of magnetite nanoparticles along z direction
(b) along x direction (c) Pt nanoparticles along z direction

Inside the Nanowire Forest

Understanding texture at nm level is crucial to foresee and design the proper electrical and transport properties of nanowire heterostructure.

III-V semiconductor nanowires are at the forefront of the solid state physics and technology (SEM image on the right). Nanowires are quasi one dimensional crystals that can be heterostructured in different sectors having different chemical composition and crystal structure. They are grown by chemical beam epitaxy (CBE) from a III-V wafer with the Au-assisted growth method. In this method the wafer is coated with a thin layer film that by a dewetting thermal treatment in the CBE chamber transforms into small Au nanoparticles.

The Au nanoparticles act as a catalyst and drive the growth of the nanowire out from the wafer. At the final stage of the growth the wafer is a forest of nanowires each with its Au nanoparticle on top
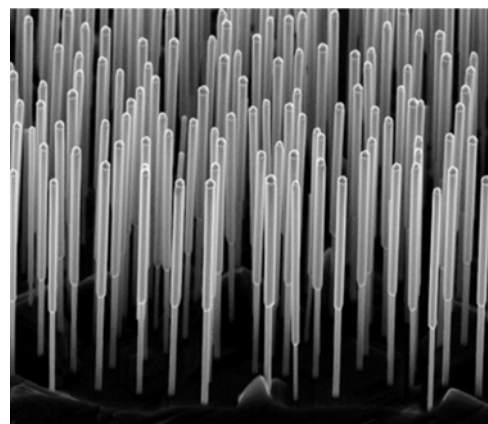
SEM image of a forest of InAs / InAsSb heterostructured nanowires

The challenge:	Distinguish structurally similar phases & perform orientation / phase of two different phases in a nanowire
Solution:	ASTAR technique coupled with precession electron diffraction

Experimental Data

TEM type: Zeiss Libra 120
Map resolution: 10 nm
Scanned area: 3 x 3 μm

Crystal Structure

InSb: Cubic, $F\bar{4}3m$
a = 0.64 Å
InAs: Hexagonal, $P6_3mc$
a= 4.27 Å c= 7.02 Å

(SEM image at the right).

The growth of heterostructured nanowires is a challenge, especially if the two crystal structures, which must be piled up on top of each other, have a large lattice mismatch. This is the case of the InAs/InAs1-xSbx/InAs heterostructure, which can only be grown in nanowires, where the strain can be relaxed at the free surface, but not in a two dimensional growth. ASTAR is able to identify where the cubic Sb sector is located between the bottom and top hexagonal InAs stems. It determines the relative orientation of the two crystal structures and is able to recognize twinned layers inside the cubic Sb sector (fig. 1).

These structural details are crucial to foresee and design the proper electrical and transport properties of the heterostructure.

figure 1
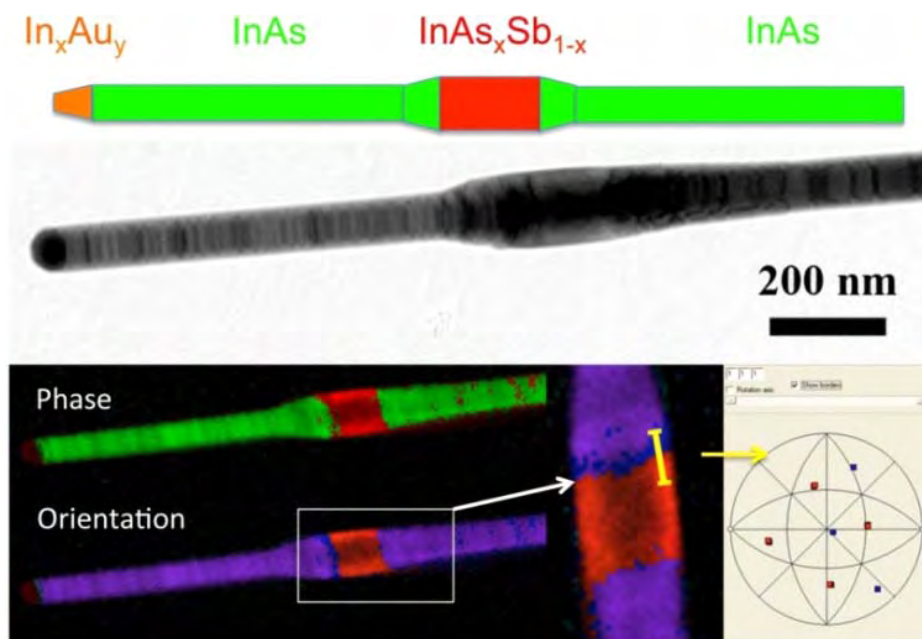
(Top) Model and bright field image of a InAs / InAs$_{1-x}$Sb$_x$/ InAs heterostructured nanowire. (Bottom) Phase and orientation mapping of the same wire. In the phase map the cubic zinc blend structure of the Sb part is identified (red) while the orientation map shows that is separated from the hexagonal wurzite. InAs stem by a twinned sector of 30 nm (blue). At the bottom left a pole figure calculated trough the twin boundary is displayed

Revealing nanoparticles texture at nm
level helps to understand
and predict their optical properties

Texture Secrets of nanoparticles

Nanoparticles are now a hot topic in several different fields for their astonishing and unusual properties compared to bulk materials. New sciences like nanochemistry, nanomedicine and nanotoxicology are born and an accurate knowledge of the nanoparticle structure is required to model properly their useful properties. Among these, the grain size, the defects and the particle shape are of major importance, since they easily correlate especially with optical properties.

The knowledge of the grain size of nanoparticles can be easily obtained with conventional TEM techniques, but the coherent domains, those inside where the structure is defect free (no twinning or grain boundaries), are much more difficult to recognize and measure.

The nanoparticle shape is another important factor to be known, since it drives the self-assembly. All these structural details call for a characterization technique that is able to furnish crystallographic information with nanometric resolution. ASTAR technique is able to supply this information.

Two examples of orientation mapping obtained by ASTAR on nanoparticles are here displayed. In fig. 1 is shown an orientation map obtained on $NaYF_4$ nanoparticles. These nanoparticles are known as upconverting, since they are able to emit visible and near-infrared light when excited with near-infrared radiation. They are very promising as fluorescent targets for biological imaging. $NaYF_4$ crystallizes in two forms one cubic and one hexagonal. ASTAR identifies all the nanoparticles as hexagonal. Those that have a hexagonal shape are oriented with the c axis (the 6 fold axis) normal to the plane, while those that are rectangular are oriented with the c axis parallel to the plane. This indicates that the nanoparticles are hexagonal prisms with a height comparable to the base sides. The second example shows an orientation map of nanogold (fig. 2).

ASTAR identifies most of the nanoparticles as oriented with the [100] direction normal to the plane, indicating that they have well developed flat {100} faces on which they fall. Some of them exhibits {111} twinning as shown by the pole figure plot at the right (fig. 2c).
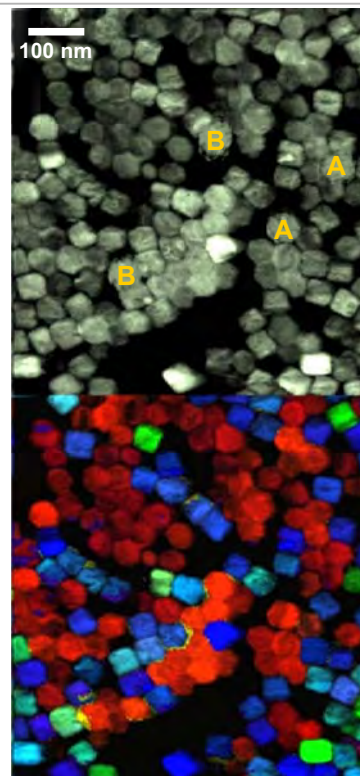
figure 1

Orientation map of $NaYF_4$ nanoparticles (Top) Index map (Bottom) Orientation map. The hexagonal (A) nanoparticles are 'red', corresponding to an orientation with the c axis normal to the plane. The rectangular (B) are 'green – blue', corresponding to orientations with the c axis on the plane.

The challenge:	Identify orientation & phase of nanoparticles with < 40 nm that crystallize in two different phases
Solution:	ASTAR technique coupled with precession electron diffraction

Experimental Data
TEM type: Zeiss Libra 120
Map resolution: 10 nm
Scanned area: 2 x 2 μm

Crystal Structure

NaYF4: Hexagonal $P\bar{6}$
a= 5.91 Å c= 3.50 Å

figure 2

Orientation map of Au nanoparticles.
a) Index map b) Orientation map
c) Pole figures of [111]. Equivalent directions of the two twins displayed in the box at the center. Most of the nanoparticles have a "red" orientation corresponding to the [100] direction parallel to the plane normal. Therefore most of them have {100} flat faces on which they fall.
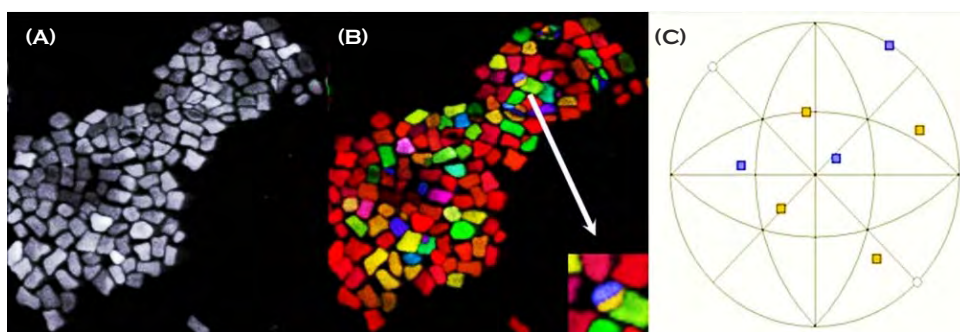
# Crystal Orientation Imaging of Organic Nanomagnets

The development and characterization of nanometer-scaled functional molecular-based materials, which may exhibit fascinating magnetic, optical or electrical properties, have recently attracted much attention. Molecular nano-objects offer the possibility of tuning or combining these properties by a rational synthetic chemical approach. These materials present promising technological applications in molecular electronics, or magneto-optic memory devices providing that we can design single domain particles with hysteresis behaviour in the future.

Nanorods of the spin crossover material $[Fe(Htrz)_2(trz)].BF_4$ are prepared by arrested growth within liquid crystal phases. A complete understanding of the crystal growth requires the identification of the orientation of the crystal axes with respect to the morphology of the nanoparticles.

$[Fe(Htrz)_2(trz)].BF_4$

nanomagnet material
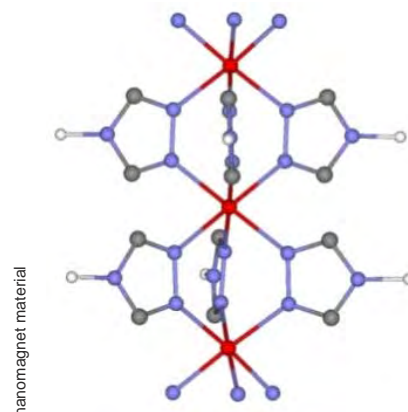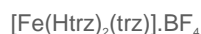
The intrinsic physical properties (magnetic and optical hysteresis) rely on the domain structure of the nanoparticle. Molecular nanoparticles of $[Fe(Htrz)_2(trz)].BF_4$ are extremely sensitive to the e-beam so that ASTAR at high frame rate is the only possible technique which allows the recording of the diffraction pattern before the destruction of the probed nanoparticle occurs.
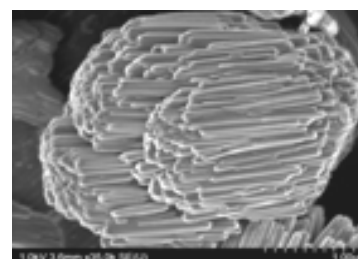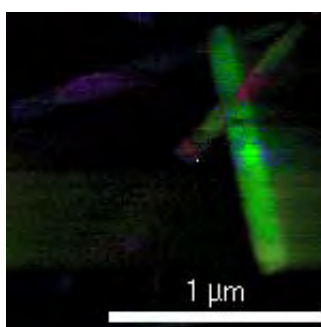

The challenge: Identify if nanocrystals diffract and whether they are single crystal particles / mapping of the unit cell disorientation along the nanoparticle.
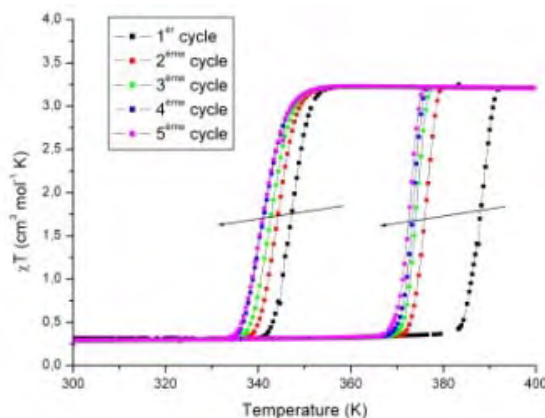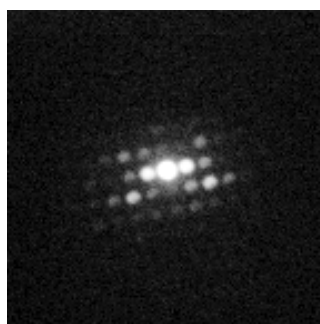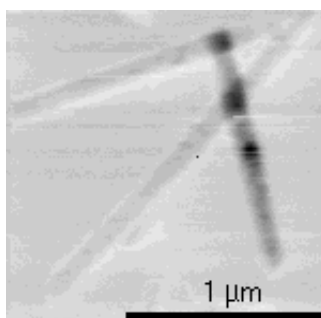
Solution: ASTAR technique at high frame rate >100 fps, no cryo-holder is used

Experimental Data
TEM type: Jeol 3010
Map resolution: 10 nm
Scanned area: 2 x 2 µm

Crystal Structure
Orthorhombic, Cmcm
a = 9.37 Å, b = 17.05 Å
c = 7.34 Å

A complete mapping of the diffraction pattern on a single nanoparticle shows that the particle is almost single domain, and that the disorientation of the crystal lattice is limited to only 5%. ASTAR also shows that the disorientation is not progressive, but rather restricted to

D. Mader et al *Journal of Dispersion Science and Technology* 32 (2011)

Nanoparticles structural identification
reveal the manufacturing process
of ancient ceramics

INSIDE A ROMAN CERAMIC FACTORY IN ANCIENT GAUL

Terra sigillata is certainly the most famous fine ware of the Roman period with characteristic decorations obtained by means of specially designed stamps (sigilla). This pottery was extensively produced in standardized shapes by a few specialized workshops and was widely distributed across the Roman Empire. Below is shown the diffusion map of one of these large workshops.

The success of this pottery was mainly because of the brightness and red color of the slip. Also in order to better understand the technical specificities of Terra sigillata, TEM and other characterization techniques have been used to investigate the microstructure and microcomposition of Roman period Terra Sigillata slips from various workshops.

A high proportion of spinel (≥25%) is characteristic of Italic productions (1st c. BC) while a high content of Fe-rich corundum(>30%) is the brand of south Gallic workshops (1st c. AC). This systematic difference is due to an evolution in the manufacturing process which permitted them to obtain a slip more resistant to the abrasion. ASTAR phase analysis indicates strongly that the ceramic sample provenance is from a factory at Graufesenque (South Gaule).
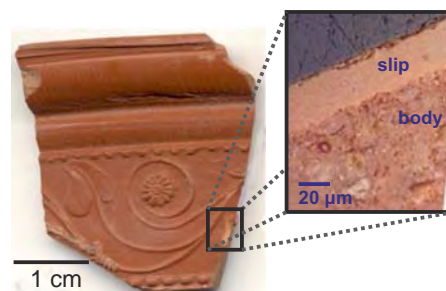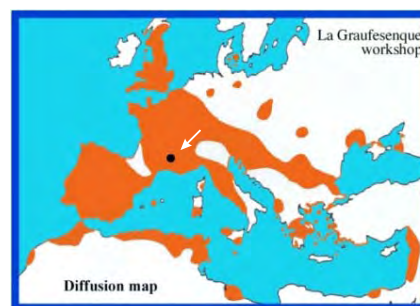

figure 1 — Fragment of a decorated cup in Terra Sigillata

The challenge:	Determine the nature, size and orientation of the different nanocrystallized phases of the slip
Solution:	ASTAR technique coupled with precession electron diffraction

Experimental Data
TEM type: CM 20 FEG
Map resolution: 2 nm
Scanned area: 2 x 2 µm

figure 2

Crystal Structure

Spinel, MgAl$_2$O$_4$: Cubic, Fd3m
a= 8.09 Å
Corindon, Al$_2$O$_3$: Hexagonal, R3c
a=4.76 Å, c=13.0 Å
Hematite, Fe$_2$O$_3$: Hexagonal, R3c
a=5.03 Å, c=13.75 Å

TOP: ASTAR high resolution phase (b) and orientation (c) maps for the crystals present in the slip of a Gallic Terra Sigillata from La Graufesenque workshop.
The slip coating consists of hematite (in red), corundum (in green) and spinel (in blue) crystals in a glass matrix (b).
In contrast with the coatings of other types of Greek and Roman potteries, there is no particular orientation of crystals.

Courtesy S. Joulié, C. Roucau & Ph. Sciau, CEMES-CNRS Toulouse, France

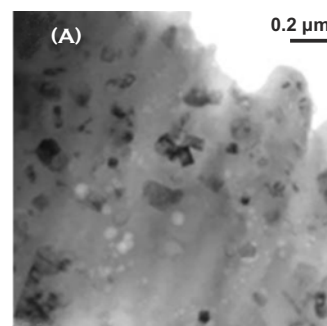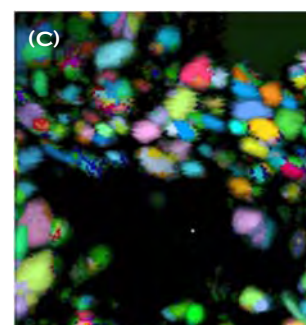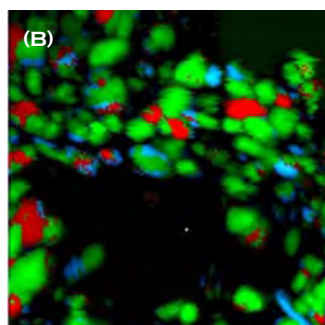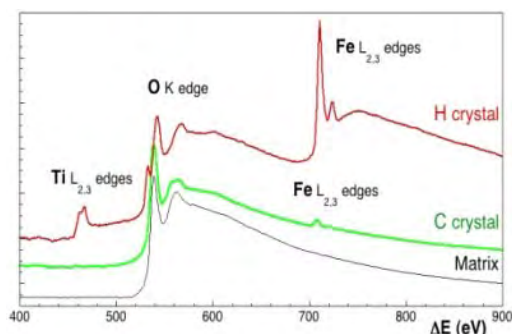LEFT: EELS analysis of the matrix, hematite and corundum crystals.

Ph. Sciau et al J. Am Cer Soc 89 (2006) 1053, Y. Leon et al JRS 41 (2010) 1550

Shed Light to Earth Seismicity

The mineral olivine dominates the composition of the Earth's upper mantle and hence controls its mechanical behaviour and seismic anisotropy. Experiments at high temperature and moderate pressure, and extensive data on naturally deformed mantle rocks, have led to the conclusion that olivine at upper-mantle conditions deforms essentially by dislocation creep with dominant [100] slip. The resulting crystal preferred orientation has been used extensively to explain the strong seismic anisotropy observed down to 250 km depth.It has been shown that this high-pressure dislocation creep produces crystal preferred orientations resulting in extremely low seismic anisotropy, consistent with seismological observations below 250 km depth.

Earthquake, Santiago, Chile, 27 October 2010

These results raise new questions about the mechanical state of the lower part of the upper mantle and its coupling with layers both above and below. In order to study the structural modifications /textures of olivine at pressures that exist at depths of 200-300 km below the surface the DIA deformation equipment coupled at Synchrotron X-Ray source was used .

As olivine is stable at ambient conditions, a post-mortem (after application of strong e.g 40 % deformation at 1373 K and 3 GPa) analysis with ASTAR in TEM has been performed in order to reveal the texture at nanoscale size.

Seismograph

The sample studied was a forsterite ; in fact , olivine is actually a name for a series between two end members, fayalite and forsterite.Fayalite is the iron rich member with a pure formula of Fe_2SiO_4. Forsterite is the magnesium rich member with a pure formula of Mg_2SiO_4. The two minerals form a series where the iron and magnesium are substituted for each other without much effect on the crystal structure. Besides the high number of defects formed during DIA deformation cycles, it has been perfectly possibly to study in detail with ASTAR the texture of the deformed sample at nm level scale.
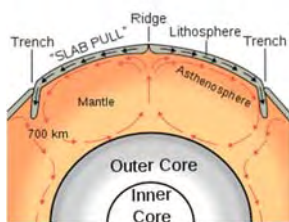
The challenge:	Identify texture and structural defects at nm scale of olivine mineral applied at very high pressures (3 Gpa)
Solution:	ASTAR technique coupled with precession electron diffraction

Experimental Data
TEM type: Jeol 3010
Map resolution: <10 nm
Scanned area: 5 x 5 µm

Crystal Structure
Olivine (Forsterite) Mg_2SiO_4:
Orthorhombic, Pbnm
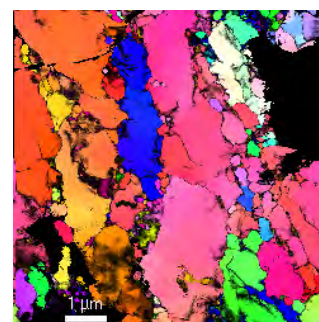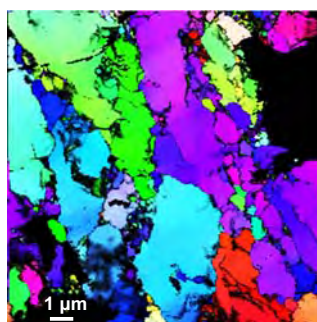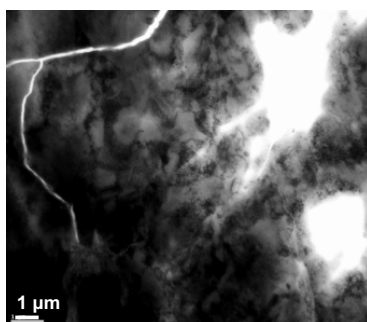a= 4.76 Å, b=10.27 Å, c= 5.98 Å

figure 1   ASTAR orientation olivine map with high number of defects (a) BF image (b) along x direction (c) Multi-Anvil Cell X-ray (X17 MAC) facility at the National Synchrotron Light Source Brookhaven USA (d) ASTAR orientation map along z direction

C. Bollinger et al *J. Appl. Cryst.* 45 (2012) 263-271

Textures of minerals at nm
are intimately linked to their physical &
chemical properties

The World of Mineral Polymorphs & Textures

Inorganic nanoparticles are widely used in catalysis. Research has led to control their morphology, crystallographic orientation and assembly. Metal oxide composites can be formed by heteroaggregation using electrostatic forces induced by the surface charges of the nanoparticles. It is important to understand the mechanisms of heteroaggregation and in particular the role of crystallographic facets.

ASTAR and TEM electron tomography has been carried out in order to analyse the

The challenge:	Identify orientation / phase of different mineral phases with particle size <50 nm
Solution:	ASTAR technique coupled with precession electron diffraction

heteroaggregates homogeneity and their 3D structure in a case study of rods of goethite (α-FeO(OH)) with particles of brookite (TiO₂) mixture. ASTAR orientation / phase map at nm scale revealed that the rods of goethite are assembled one to each other along their long edges. Particles of brookite are agglomerated and are linked to the tips of the goethite rods (fig.1). It is very important that exactly the same results have been revealed using TEM electron tomography. It is interesting to observe dramatic resolution in ASTAR phase maps generated with Cs corrected TEM in comparison with std Lab6 300 kV TEM (Jeol 3010) Fig.1a-b

Emphasis on the synthesis of nanoparticles is currently directed at designing their crystal structure and morphology and therewith their self-assembling behavior. We employed nonionic water-in-oil microemulsions as reaction medium to explore nanoscopic crystallization pathways for barium carbonate (witherite mineral).

Contrary to what was originally expected is the genesis of stable orthorhombic witherite in these media is not a straightforward process enabling thus the investigation of birth, deterioration and transformation of so far unprecedented metastable amorphous and crystalline nanoparticles. ASTAR gives the opportunity to identify the different polymorph phases in a crystalline nanoparticle ensemble (orientation/phase maps) and to determine major growth directions of individual nanoparticles or the adjacent faces of self-assembled nanoparticles (orientation maps) thus gaining deeper insight into the underlying processes. Fig. 2 shows monoclinic (P12₁/m1 (11)) nanocubes together with orthorhombic (Pnma (62)) nanorods that have grown out in a direction.
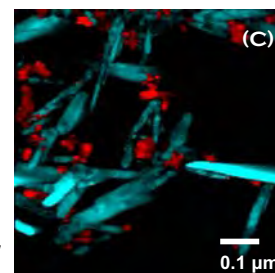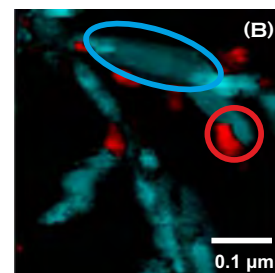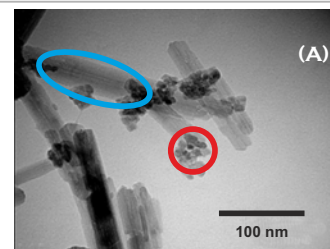
figure 1

■ Bank [Brookite] 100_ 0.2
■ Bank ['Goethite' Pnma]

(A) Brookite particles & Goethite nanorods TEM bright field image
(B) ASTAR phase map of the same area
(C) ASTAR phase map with <nm resolution taken with aberration corrected Cs-TEM
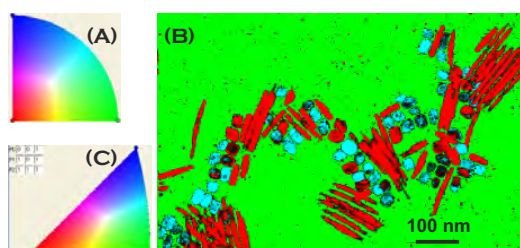
Crystal Structure

TiO₂ Brookite: Orthorhombic, Pbca
a= 9.17 Å, b= 5.44 Å, c= 5.13 Å
(α-FeO(OH))Goethite: Orthorombic, Pbnm
a= 4.59 Å, b= 9.95 Å, c= 3.02 Å
Whiterite BaCO₃: Orthorhombic, Pnma
a=5.31 Å, b= 8.9 Å, c= 6.43 Å
BaCO₃: Monoclinic, P2₁/m
a = 6,9 Å, b= 5,29 Å , c = 4,51 Å; β= 107,8°

Experimental Data

TEM type: Libra 200 FE Cs(**Fig.1c**)
Map resolution: <1 nm
Scanned area: 2 x 2 µm

TEM type: Tecnai 20 F (**Fig.2**)
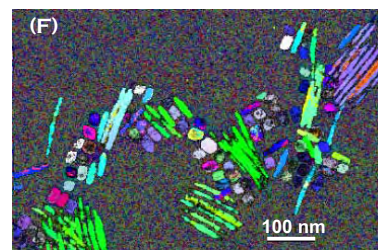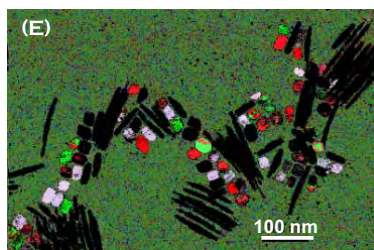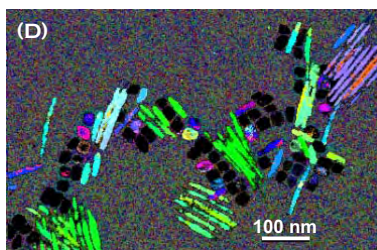Map resolution: 1 nm
Scanned area: 800 x 600 nm

figure 2

ASTAR   phase map of different whiterite polymorphs (blue-monoclinic, red ortho BaCO₃) (b) colour code for orthorhombic structure (a) and for monoclinic
(c) ASTAR orientation map for BaCO₃ orthorhombic phase (y axis), (d) same for BaCO₃ monoclinic phase (z axis) (e) ASTAR   orientation map for both BaCO₃ polymorphs (y axis)

Design Materials with Specific Applications
Technical details: ASTAR - Jeol 2100F; precession angle 0.7°
Research Group: Dr. Dong Qui, Univ. of Queensland, Australia; Dr. P. Cizek, Dr. A. Sullivan, Deakin Univ., Australia

Better Steel with Improved Properties
Technical details: CM 200 - ASTAR; precession angle 0.5°
Research Group: Dr. A. Gholinia, Dr. S. Height, Univ. of Manchester, UK

Challenging Materials for Challenging Applications
Technical details: Tecnai F20 - ASTAR; precession angle 0.5°
Research Group: Dr. S. Lartigue, CNRS, Paris, France; Dr. M. Veron, INP Grenoble, France

Steel Corrosion in Nuclear Plants
Technical details: Tecnai F20 - ASTAR; precession angle 0.6°
Research Group: Dr. F. Delabrouille, EDF Paris, France

Structure of Embedded Nanodomains in Intermetallics
Technical details: Rotational tomographic holder; beam precession (1.2°) by DigitStar, NanoMEGAS.
Research Group: Prof. U.Kolb, Dr. E.Mugnaoli, Johannes Gutenberg-Universität, Mainz, Germany; Prof. N.Frangis, Dr. E.Sarakinou, Univ of Thessaloniki, Greece

Metals Under Huge Stress
Technical details: Tecnai F20 - ASTAR
Research Group: Dr. C. Kuebel, D. Wang, KIT Karlsruhe, Germany

Pavements of the Nanoworld
Technical details: ASTAR - Jeol 3010; precession angle 0.8°
Research Group: Dr. P. Cizek, Dr. A. Shelivan,Deakin Univ., Australia,

Understanding Li Insertion for Next Generation Batteries
Technical details: Jeol 2200 FF - ASTAR; precession angle 1.2°
Research Group: Dr. G. Brunetti, Dr. J. L. Rouviere, CEA-LETI Grenoble, France

Nanoscale Reaction Models in Solid Oxide Fuel Cells
Technical details: Jeol 2200 FS - ASTAR; precession angle 0.7°
Research Group: Dr. M. Cantoni, Dr. A. Duncan, EPFL Lausanne, Switzerland, Dr. M. Veron, INP Grenoble, France

Atomic Scale of Nanolayer Composites
Technical details: Jeol 2100F - ASTAR; precession angle 0.6°
Research Group: Dr. P. Cizek, Deakin Univ., Australia; Dr. Bhattacharyya, ANSTO, Australia; Dr. M. Veron, INP Grenoble, France

Next Generation Circuits for Semiconductor Industry
Technical details: Jeol 2100F - ASTAR; precession angle 0.7°
Research Group: Prof. P. Ferreira , Dr. A. Darbal , Dr. J. Ganesh , Dr. J. Kameswaran , Dr. S. Rajashekara, Univ. of Texas at Austin, Prof. K. Barmak ,Dr. G. S. Rohrer, Carnegie Mellon University

Structure of Magnetic Semiconductors
Technical details: Jeol 2200 FS - ASTAR; precession angle 0.5°
Research Group: Dr. H. Kirmse, Dr. I Hausler, Humboldt Univ., Berlin, Germany

Hybrid Inorganic / Organic Systems for Optoelectronics in Daily Life
Technical details: Jeol 2200 FS - ASTAR; precession angle 0.5°
Research Group: Dr. H. Kirmse, Dr. I Hausler, Humboldt Univ., Berlin, Germany

Drug Delivery & Structure of Nanoparticles
Technical details: Tecnai 20 FS - ASTAR; Tecnai F20 - ASTAR; Jeol 2100F - ASTAR; precession angle 0.7°
Research Group: Dr. Hui Hu, Univ. of Singapore; Dr. S. Rouvimov, Dr. P. Moeck, Portland State Univ. USA, Dr. P. Ferreira, Texas Univ. at Austin, USA

Inside the Nanowire Forest
Technical details: Zeiss Libra 120 – ASTAR
Research group : Dr. M. Gemmi, Italian Institute of Technology Pisa, Dr. l. Sorba CNR Nano, Pisa , Dr. D. Ercolani Scuola Normale Superiore Pisa, Italy

Texture Secrets of Nanoparticles
Technical details: Zeiss Libra 120 – ASTAR /
Research Group: Dr. M. Gemmi (CNI@NEST, Istituto Italiano di Tecnologia, Pisa, Italy), V. Voliani (NEST, Scuola Normale Superiore, Pisa, Italy

Crystal Orientation Imaging of Organic Nanomagnets
Technical details: Jeol 3010-ASTAR
Research group: Dr. S.Pillet Univ of Nancy, Dr. E.Rauch, M.Veron INP Grenoble, France

Inside a Roman Ceramic Factory in Ancient Gaul
Technical details: CM 20 FEG-ASTAR
Research group: Dr. P.Sciau CEMES Toulouse, France

Shed Light to Earth Seismicity
Technical details: Jeol 3010- ASTAR Precession angle 0.8°
Research group: Dr. Bollinger , Prof. P. Cordier, Univ of Lille, Dr. E. Rauch, M. Veron, INP Grenoble, France

The World of Mineral Polymorphs & Textures
Technical details: Libra 200 FE Cs – ASTAR & Tecnai 20F –ASTAR Precession angle 1°
Research group: Dr. E. Rauch, INP Grenoble, France, Dr. T. Weirich, Dr. Wiebke, Sager RWTH Univ of Aachen, Germany & Prof. M. Veron INP Grenoble, France

NanoMEGAS
Advanced Tools for electron diffraction

NanoMEGAS SPRL

Blvd Edmond Machtens 79

B-1080 Brussels

Belgium

www.nanomegas.com

info@nanomegas.com